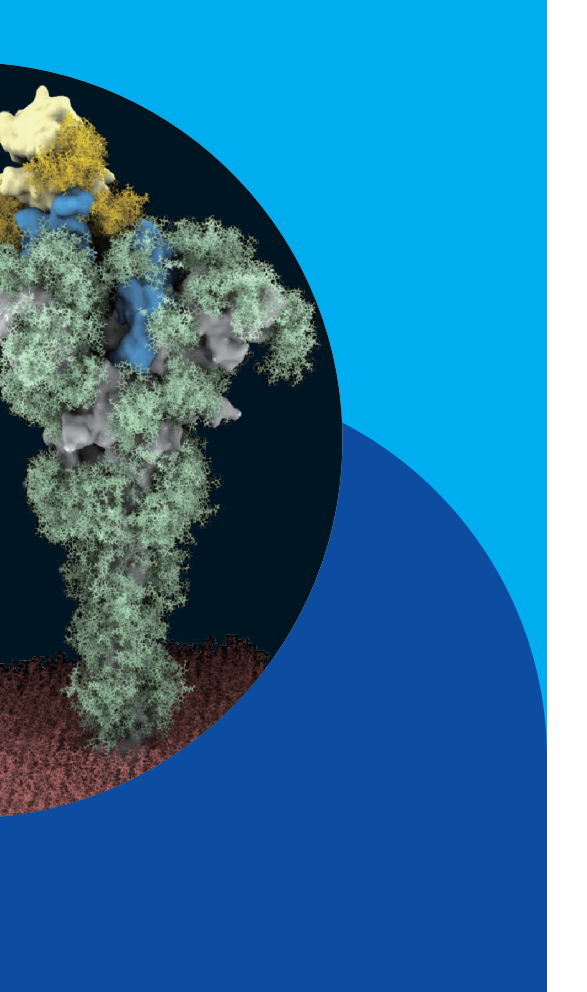
Soft Matter



Soft-matter science covers a diverse range of materials, including polymers, colloids, liquid crystals, biomacromolecules, and self-assembled systems. These materials exhibit hierarchical structures and dynamic behaviors that require advanced characterization techniques to unravel their complex properties. Synchrotron radiation provides powerful tools for probing soft matter at multiple length scales, offering high-resolution insights into their structure, interactions, and functional properties.

Several beamlines are dedicated to soft-matter research at the Taiwan Photon Source (TPS) and Taiwan Light Source (TLS). **TPS 13A** biological small-angle X-ray scattering (BioSAXS) enables structural analysis of biomacromolecules in solution. **TPS 44A** quick-scanning X-ray absorption spectroscopy provides element-specific insights into local electronic and atomic structures. **TLS 23A1** small/wide-angle X-ray scattering facilitates the characterization of hierarchical architectures in polymers, biomaterials, and nanostructured systems.

This section presents four recent studies that demonstrate the versatility of synchrotron techniques in soft-matter research. The first study investigated glycoprotein structures by using **TPS 13A** BioSAXS combined with computational modeling to characterize the conformational properties of highly glycosylated proteins. The findings offer insights into glycan-mediated interactions and their role in biological functions. The second study explored centrosome regulation during cell division, focusing on the phase separation of Cep57 and its role in microtubule nucleation. **TPS 13A** BioSAXS helped elucidate the molecular mechanisms governing centrosomal organization and its impact on cellular processes.

The third study examined the aqueous-phase crystallization of metal-organic frameworks, with **TPS 13A** *in situ* SWAXS providing real-time tracking of nucleation and growth mechanisms. The results revealed how biomolecules influence framework formation, shedding light on biomimetic strategies for sustainable material synthesis. The fourth study focused on the stabilization of single platinum atoms within silicate nanochannels for enhanced catalytic efficiency. **TPS 44A** X-ray absorption spectroscopy was used to confirm atomic coordination environments, while **TLS 23A1** and **TPS 13A** were utilized to aid analysis of the hierarchical structure and dispersion of Pt atoms.

These studies exemplify how synchrotron-based techniques enable a deeper understanding of soft-matter systems, providing essential structural and functional insights. The ability to probe nanoscale architectures with high precision continues to drive advances in biomaterials, catalysis, and fundamental science, paving the way for future discoveries and technological applications. (by Orion Shih)

Advancing Glycoprotein Insights: Bridging Glycobiology and Structural Biology

Protein glycosylation is integral in biology; however, quantitative annotation of the structure-function relationship of glycosylation is challenging. This article reports the findings of an interdisciplinary and international team formed to tackle this challenge.

The surfaces of cells and viruses are often coated with a thick layer of sugar (also known as glycans), presenting a challenge for identifying specific proteins or biomolecules within this complex environment. In nature, however, efficient biomolecular interactions take place within this forest of glycans. Most extracellular proteins are post-translationally modified by glycans with varying sizes and complexity. The masking effect of these glycans allows bacteria and viruses to evade recognition and attack by the host immune system.

Structural biology focuses on providing pivotal structural information at an atomic resolution to help to understand the mechanisms governing biological functions. Such an underlying principle is also used by the immune system, where antibodies recognize the structural characteristics of foreign substances, such as antigens, to achieve immune protection. Nevertheless, structural biology encounters two technical challenges when examining the intricate structures of protein glycans. First, glycan molecules have a complex chemical composition, and their biosynthesis lacks a one-to-one template. Second, glycans are highly dynamic, making it challenging to accurately define three-dimensional spatial distributions. Therefore, the intrinsic microscopic compositional and conformational heterogeneity presents a fundamental challenge to the accurate modeling of glycan structures.

The research team led by Shang-Te Danny Hsu (Academia Sinica) tried to solve this problem from the structural understanding of protein glycosylation started in 2018 through a collaboration with Hui-Wen Chang at the National Taiwan University and Kay-Hooi Khoo at Academia Sinica. They used cryo-electron microscopy (cryo-EM) to determine the near-atomic structure of the spike protein of a type I feline infectious peritonitis virus (FIPV).¹ They identified an exceptionally well-defined cryo-EM map enabling the modeling of one of the longest N-glycan structures in the literature. The atomic model of the fully glycosylated FIPV spike protein was built manually using the information derived from mass spectrometry (MS) analysis. Nonetheless, the data analysis and model building are laborious and not very quantitative.

To address these issues, they collaborated with Khoo to develop a robust workflow to quantitatively characterize the N-glycosylation profiles of the spike proteins of SARS-CoV-2 variants.² They also determined the cryo-EM structures of the same spike proteins, with an emphasis on recovering structural information of glycans. They further collaborated with Cyril Hanus at the Inserm, France, and Mateusz Sikora at the Max Planck Institute of Biophysics, Germany, to develop the computational tool called GlycoSHIELD³ to integrate the experimental observables with computational modeling to automate the process of model building of glycoproteins (Fig. 1). Such a procedure can be accomplished using a personal computer in minutes rather than using a high-performance computing center for full-blown all-atom molecular dynamics simulations of fully glycosylated spike proteins solvated in an explicit solvent model. Additionally, GlycoSHIELD offers predictive powers for identifying potential receptor binding sites and antigenic targets for therapeutic purposes based on the common characteristic that the less-shielded protein surfaces are generally more likely to be used for host receptor binding and targeted by neutralizing antibodies.

Small-angle X-ray scattering (SAXS) is exceptionally versatile in describing protein structures and dynamics in solution. The research team has benefited tremendously from the support of the biological SAXS **TPS 13A** beamline research team at the NSRRC. In the context of GlycoSHIELD, they used SAXS to characterize two highly glycosylated proteins, namely, the extracellular domains (ECDs) of N-cadherin pertinent to cell–cell adhesion and

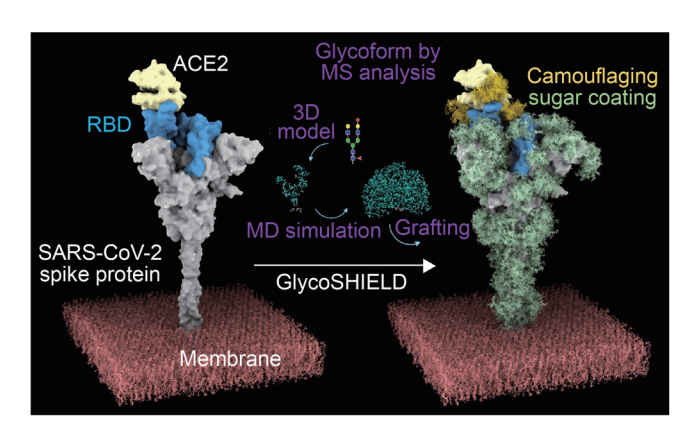


Fig. 1: Schematic overview of the principle of GlycoSHIELD.

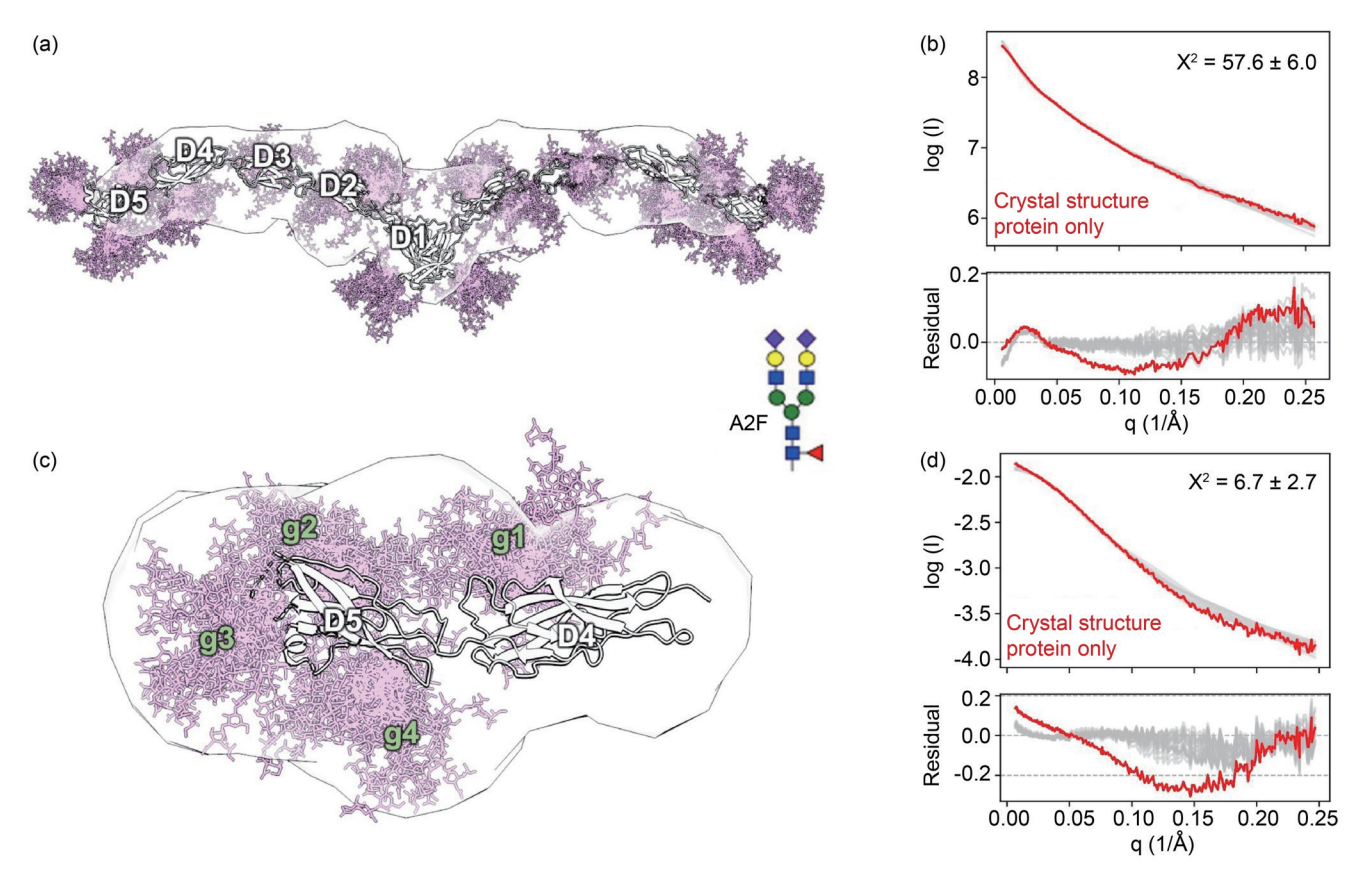


Fig. 2: SAXS analysis of N-cadherin variants. (a) The molecular envelope of N-cadherin ECD 1-5 (D1-D5) in a seagull-like homodimeric assembly. The crystal structure, indicated by a white outline, is modified with a biantennary complex type (A2F) N-glycan in its putative N-glycosylation sites, which are indicated by pink sticks. (b) The experimental SAXS profile is superimposed with the back-calculated SAXS profiles based on the crystal structure (red) and the additional N-glycan structures in 20 different conformations (gray). The residuals are shown below the SAXS profiles. Similar structural representations of the D4 and D5 of N-cadherin are shown in (c), and the corresponding SAXS data analyses are shown in (d). [Reproduced from Ref. 3]

the ECD of the receptor-like protein tyrosine phosphatase (PTPRA), which is crucial for transmitting extracellular signals to trigger intracellular chemical reactions.

N-cadherin is a calcium-binding glycoprotein comprising five folded ECDs (Fig. 2(a)). Molecular dynamics simulations have shown that glycosylation is important for maintaining the extension of N-cadherin. However, most of the glycans are removed to solve the crystal structure of N-cadherin, which is an intrinsic issue in protein crystallography. The team used SAXS to demonstrate that the fully glycosylated N-cadherin variants indeed adopt an extended seagull-like dimer structure, which is consistent with the crystallographic finding (Fig. 2(a)). By modeling different glycan ensembles onto the putative N-glycosylation sites, they could further improve the agreement between the experimental and back-calculated SAXS profiles based on the atomic ensemble structures. This illustrates how the combination of GlycoSHIELD modeling and experimental SAXS inputs can generate a more realistic glycoprotein conformational ensemble (Figs. $2(a)-2(d)).^3$

Structural analysis of highly glycosylated intrinsically disordered proteins represents an even more significant

challenge to structural biology. In collaboration with Khoo and his colleagues, they comprehensively profiled the glycosylation of the PTPRA-ECD, which comprises only 120 amino acids with four N-glycosylation sites and over 30 O-glycosylation sites. Using the SAXS data derived from the PTPRA-ECD fused to a dimeric Fc scaffold and GlycoSHIELD, the team generated an ensemble structure with the N- and O-glycans decorating PTPRA-ECD to account for the spatial occupancy by the N- and O-glycans (Fig. 3). They further collaborated with Takayuki Uchihashi at Nagoya University in Japan to directly visualize the opening and closing states of the PTPRA-ECD through high-speed molecular force microscopy to confirm the bottlebrush-like molecular envelope of PTPRA-ECD inferred by SAXS. This interdisciplinary exercise underscores the importance of an integrated structuralbiology approach to characterize such a highly complex and dynamic system.4

The current modeling algorithm of GlycoSHIELD is limited to the steric effect of glycan ensemble structures on the protein of interest. An improved algorithm is required to account for the non-covalent interactions. Furthermore, the compositional heterogeneity of the individual glycosylation sites presents a combinatorial problem of a large number

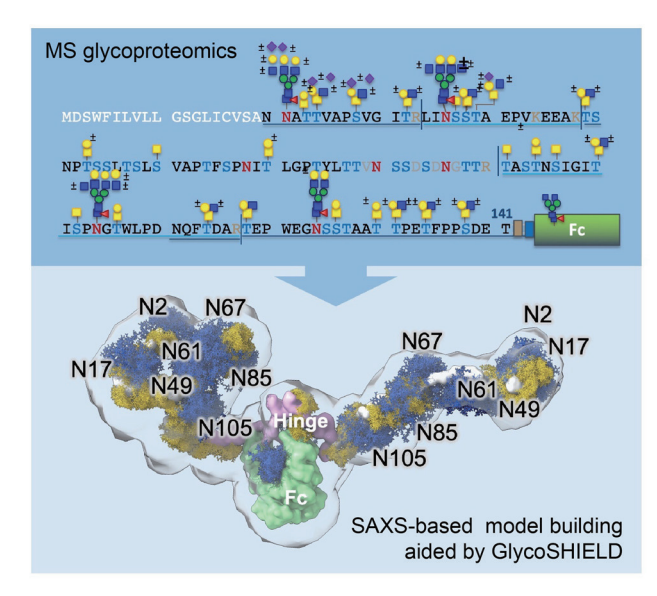


Fig. 3: Integrated structural analysis of the densely N- and O-glycosylated and intrinsically disordered PTPRA-ECD fused to Fc. The representative N- and O-glycoforms derived from MS analysis are shown on the top, and the atomic model of the fully glycosylated protein structure is shown below. The N- and O-glycans are shown in blue and yellow, respectively. The molecular envelope of the Fc-fused PTPRA-ECD is shown on a transparent surface. [Reproduced from Ref. 4]

of overall glycosylation patterns that one should consider when describing the physicochemical properties of the protein of interest at an atomic level. The optimization of GlycoSHIELD's molecular models and experimental observations is necessary to achieve a balance between the computational performance and the completeness of experimental observations while ensuring that the molecular models of glycoproteins comply with the basic laws of physics and chemistry, an area that will require further explorations. (Reported by Shang-Te Danny Hsu, Academia Sinica)

This report features the work of Shang-Te Danny Hsu and his collaborators published in Cell **187**, 1296 (2024), and the work of Kay-Hooi Khoo and his collaborators published in JACS Au **3**, 1864 (2023).

TPS 13A Biological Small-angle X-ray Scattering

- Biological Small/Wide Angle X-ray Scattering
- Biological Macromolecules, Protein Solution, Life Science

References

- T. J. Yang, Y. C. Chang, T. P. Ko, P. Draczkowski, Y. C. Chien, Y. C. Chang, K. P. Wu, K. H. Khoo, H. W. Chang, S.-T. D. Hsu, PNAS 117, 1438 (2020).
- 2 C. W. Kuo, T. J. Yang, Y. C. Chang, P. Y. Yu, S.-T. D. Hsu, K. H. Khoo, Glycobiology. 32, 60 (2022).
- Y. X. Tsai, N. E. Chang, K. Reuter, H. T. Chang, T. J. Yang, S. von Bülow, V. Sehrawat, N. Zerrouki, M. Tuffery, M. Gecht, I. L. Grothaus, L. C. Ciacchi, Y. S. Wang, M. F. Hsu, K. H. Khoo, G. Hummer, S.-T. D. Hsu, C. Hanus, M. Sikora, Cell 187, 1296 (2024).
- 4. Y. C. Chien, Y. S. Wang, D. Sridharan, C. W. Kuo, C. T. Chien, T. Uchihashi, K. Kato, T. Angata, T. C. Meng, S.-T. D. Hsu, K. H. Khoo, JACS Au 3, 1864 (2023).

The Key to Accurate Cell Division: Centrosome Regulation

Cep57 regulates centrosome maturation and microtubule nucleation via phase separation, ensuring accurate cell division.

Liquid-liquid phase separation (LLPS) is a process driven by multivalent interactions among biomolecules, such as proteins and nucleic acids, forming dense, dynamic structures known as biomolecular condensates. Recent evidence supports LLPS as a fundamental organizing principle for membrane-less organelles. The centrosome, consisting of a pair of centrioles surrounded by pericentriolar material (PCM), plays a crucial role in regulating cell division. As cells prepare for mitosis, the centrosome undergoes a maturation process characterized by the expansion of the PCM and an increase in its microtubule nucleation capacity by recruiting centrosomal scaffolding proteins and microtubule nucleation factors. This facilitates the assembly of the mitotic spindle and ensures the precise segregation of chromosomes during mitosis.

Human Cep57 is a coiled-coil scaffold protein located in the inner layer of the PCM and controls the process of centriole duplication and centrosome maturation for faithful cell division. Cep57 truncation mutations are genetically linked to mosaic-variegated aneuploidy syndrome, which features centrosome amplification and aberrant spindle formation. However, the molecular mechanisms by which Cep57 regulates PCM organization and microtubule assembly remain unknown. Phase separation has been implicated in some key centrosomal scaffolds, such as SPD-5 (a human CDK5RAP2 functional homolog) and the Cep63/Cep152 complex. During interphase, Cep57 forms a complex with the middle layer scaffold Cep63 and Cep152, serving as regulators for centrosome maturation. However, it is unclear whether Cep57 undergoes phase separation and how these centrosomal scaffolding components coordinate to organize the centrosome.

To address these questions, the research team led by Hui-Chun Cheng at National Tsing Hua University employed various analytical techniques and successfully demonstrated that Cep57 assembles into micron-sized biomolecular condensates through LLPS driven by multivalent interactions. Blocking multivalent interactions on Cep57 induced centrosome amplification in the cells. Furthermore, Cep57 condensates were found to facilitate microtubule nucleation by concentrating α/β -tubulin in the condensates. Finally, a novel molecular interplay was observed between the centrosomal scaffold, which is the negative regulation of Cep63 on LLPS, and the microtubule nucleation activity of Cep57. The following report briefly presents their results.

Cheng's team observed that overexpression of Cep57 forms spherical puncta in cells and some of them colocalized with microtubules (**Fig. 1(a)**). To study the molecular mechanism of the puncta formation, they purified Cep57 and found that Cep57 is highly soluble in high salt conditions (1 M NaCl) but self-assembles into micron-sized spherical droplets with liquid-like properties when salt was reduced to 200 mM (**Fig. 1(c)**).

As full-length Cep57 is prone to degradation, a Cep57S construct was created, which has similar properties to Cep57 but allows for higher protein quality to perform biochemical and biophysical characterization (**Fig. 1(b)**). To identify the regions responsible for LLPS, the N-terminal and C-terminal fragments of Cep57 were expressed and purified. It was found that both terminals are necessary for condensate formation. As it was observed that the phase separation of Cep57 is salt-dependent, electrostatic interactions were speculated to play a role in phase separation. Mutagenesis analysis revealed a highly conserved K/R motif located in the C-terminal direction from the NTD, which also contributes to the phase separation of Cep57S. The combined data showed that the NTD, CTD, and K/R motifs contribute to the phase separation of Cep57S.

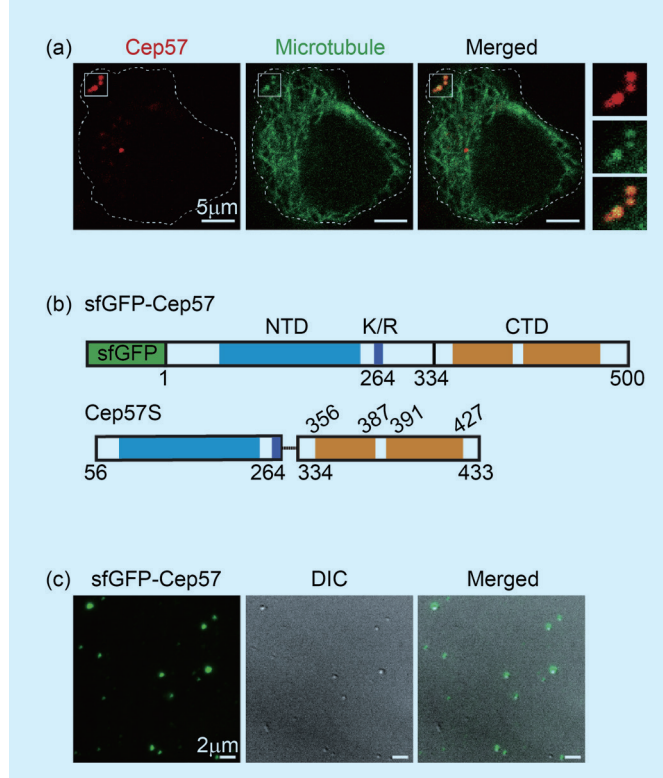


Fig. 1: Human Cep57 undergoes liquid–liquid phase separation under physiological conditions. (a) Confocal images of HeLa cells co-expressing Cep57-mCherry (red) and Neon-MAP4m as the microtubule marker (green) for 16 h. (b) Domain organization of sfGFP-Cep57 and Cep57S. Coiled-coil N-terminal domain (NTD), blue; coiled-coil C-terminal domain (CTD), orange; poly-K/R motif (K/R), dark blue. Cep57S is composed of residues 56 to 264 fused to 334 to 433. (c) TIRF images of sfGFP-Cep57 droplets. The sfGFP-Cep57 (25 nM) were visualized 4 h after condensation in low salt (200 mM NaCl). [Reproduced from Ref. 1].

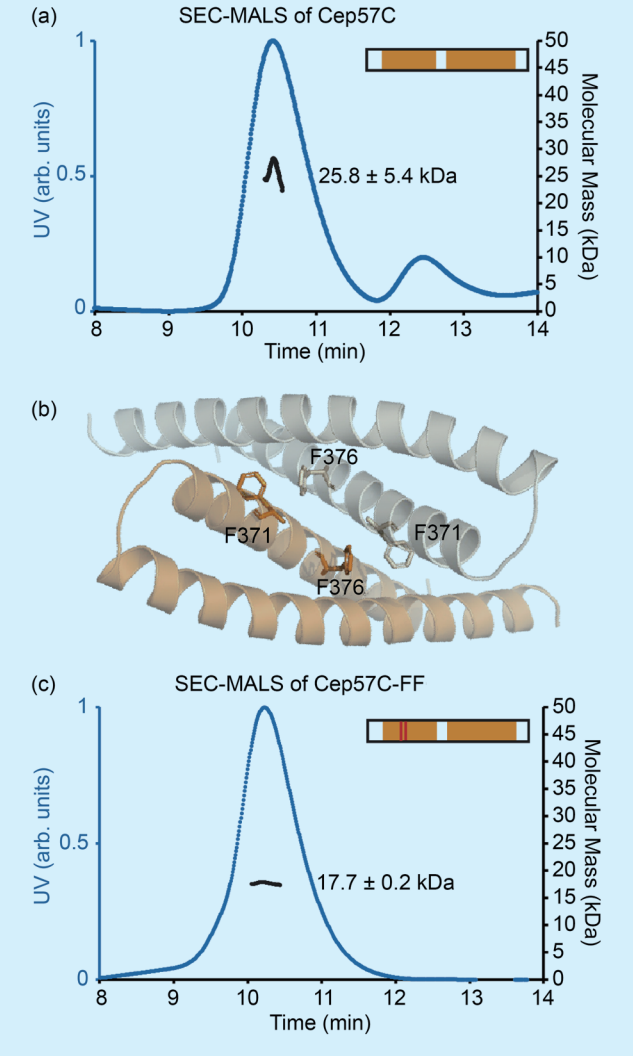


Fig. 2: CTD dimerization facilitates phase separation of Cep57. (a) SEC-MALS profile of Cep57C. The calculated molecular mass for Cep57C is 12.5 kDa. (b) The crystal structure of Cep57C is shown as a dimer. The side chains of F371 and F376 are in stick presentation. (c) SEC-MALS profile of Cep57C-FF. [Reproduced from Ref. 1]

From the SEC-MALS analysis and crystal structure of Cep57C, Cheng's team showed that Cep57C, which adopts a helix-turn-helix fold, forms a symmetric dimer with residues F371 and F376 at the dimer interface (**Figs. 2(a) and 2(b)**). When these two residues were mutated to alanines in the Cep57S-FF mutant, the dimer formation was weakened (**Fig. 2(c)**), and the phase separation ability decreased. Therefore, Cep57C dimerization is essential to promote Cep57 condensation.

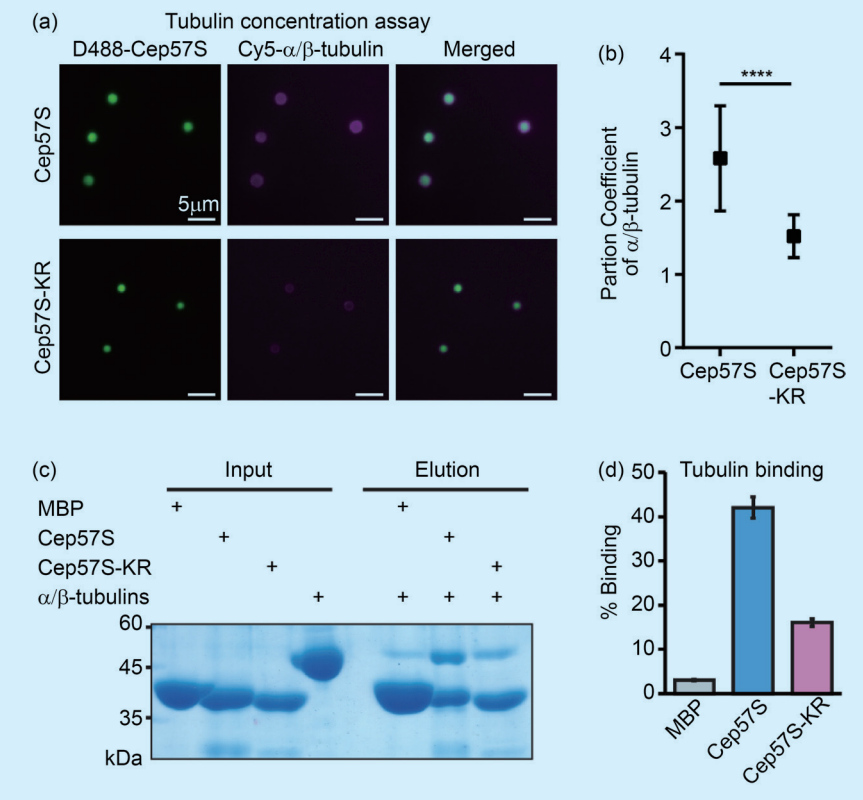


Fig. 3: The Cep57 scaffold concentrates α/β -tubulin for microtubule assembly. (a) D488-Cep57S or D488-Cep57S-KR condensates with Cy5-tubulin dimers in 66 μM nocodazole. Images were taken 20 min after the addition of tubulin. (b) Quantification of the α/β -tubulin partition coefficient to Cep57S (n = 69) or Cep57-KR (n = 76) condensates in experiments from panel (a) pooled from three repeats. [*****] p < 0.0001. Data represent mean ± SD. (c) His-tag pull-down assay of tubulin with His-Cep57S and His-Cep57S-KR. His-MBP was used as the negative control. Quantification of binding of α/β -tubulin in experiments. The percentage of binding was defined as the intensity of tubulin in the eluent divided by the intensity of the loaded sample (N = 3). (d) Percentage of cells with centrosomal microtubule asters in the microtubule regrowth experiments. HeLa cells were sequentially transfected from left to right with negative control siRNA + empty vector, Cep57 siRNA + empty vector, Cep57 siRNA + Cep57, and Cep57 siRNA + Cep57-KR. Each data point was derived from observations of 100 to 200 cells. [*] p < 0.05; [**] p < 0.01. N = 3. [Reproduced from Ref. 1]

Cep57S condensates were also found to concentrate α/β -tubulin by about 2.6-fold to promote microtubule polymerization inside the Cep57S condensates (**Figs. 3(a) and 3(c)**). The *in vitro* pull-down assay revealed that the K/R motif is the tubulin binding site. A siRNA rescue experiment with the Cep57S-K/R mutant demonstrated that Cep57 plays a role in centrosomal microtubule organization in a K/R motif-dependent manner (**Figs. 3(c) and 3(d)**).

The research shows that Cep63 prevents the LLPS and microtubule nucleation functions of Cep57S. When Cep57S formed co-condensates with Cep63, the ability to concentrate α/β -tubulin was decreased (**Fig. 4(a)**). Additionally, both the condensate size and partition coefficient of Cep57S decreased as the concentration of Cep63N, the Cep57 binding domain, increased (Figs. 4(b) and **4(c)**). SAXS measurements taken at the TPS 13A beamline showed that the fractal network of Cep57S was diminished by the addition of Cep63N, further suggesting that Cep63 dissolves Cep57S condensates by disrupting the network structure (**Fig. 4(d)**). Collectively, these results

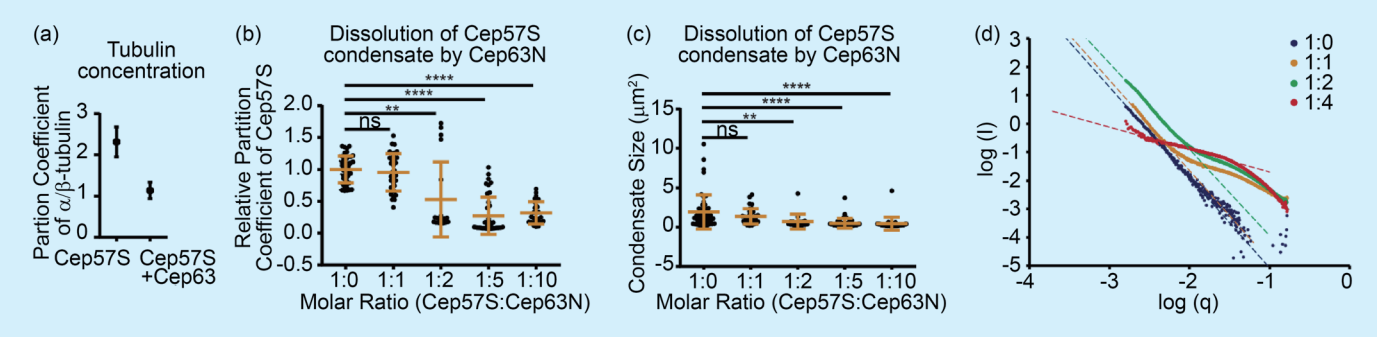


Fig. 4: Cep63 inhibits Cep57's LLPS and function. (a) The partition coefficient of α/β -tubulin in Cep57S or Cep57S–Cep63 condensates. n=51 (Cep57) and n=102 (Cep57S–Cep63) pooled from three independent experimental repeats. (b,c) Partition coefficient and size analysis of Cep57S condensates with increasing concentrations of MBP-Cep63N. The concentration of Cep57S was fixed at 2 μ M. Data from two independent experiments were pooled for quantification; n=51 (1:0), n=34 (1:1), n=19 (1:2), n=39 (1:5), and n=28 (1:10). (d) SAXS profile of Cep57S fixed at 10 μ M in the presence of MBP-Cep63N at indicated ratios (Cep57S:MBP-Cep63N). Proteins were incubated at 22 °C for 12 hours before the SAXS experiments. The dotted line represents extrapolation of the linear regression of scattering data in the q range from 0.01 Å-1 to 0.002 Å-1 or 0.01 Å-1 to 0.006 Å-1 (for 1:1 only). Slopes for linear regression were -3.2 (1:0), -3.2 (1:1), -3.0 (1:2), and -0.8 (1:4). As MBP-Cep63N increased, the absolute value of the slope decreased, implying that the complexity of the structure decreased. [Reproduced from Ref. 1]

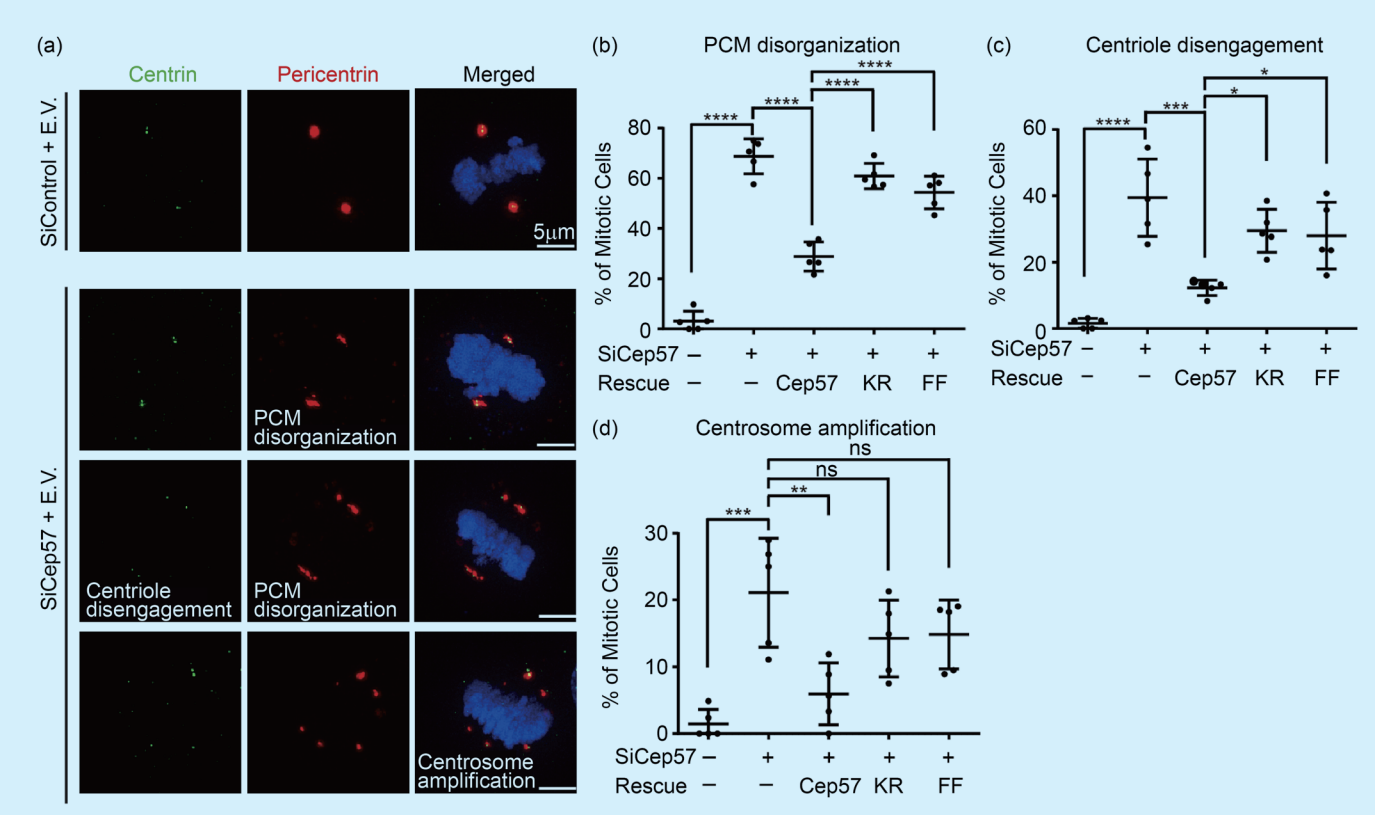


Fig. 5: Multivalent interactions of Cep57 regulate the structure and number of human centrosomes. (a) Fluorescence images of mitotic HeLa cells sequentially transfected with negative control siRNA and mCherry empty vector, or Cep57 siRNA and mCherry empty vector. Centrin, green; pericentrin, red; DNA, blue. (b–d) Percentage of mitotic cells with indicated phenotypes. HeLa cells were sequentially transfected from left to right with negative control siRNA + mCherry empty vector, Cep57 siRNA + mCherry empty vector, Cep57 siRNA + Cep57-mCherry, Cep57 siRNA + Cep57-KR-mCherry, and Cep57 siRNA + Cep57-FF-mCherry, followed by synchronization. Each data point was collected from 30 to 50 mitotic cells. N = 5. [*] p < 0.05, [**] p < 0.01, [***] p < 0.001, and [****] p < 0.0001. [Reproduced from Ref. 1]

suggest that modulating LLPS of Cep57 by Cep63 serves as a mechanism to regulate the structural expansion and functional activity of the PCM scaffolding proteins.

Finally, cell assays with Cep57-FF and Cep57-KR mutants were performed to examine the functional significance of Cep57 in centrosome duplication. Depletion of endogenous Cep57 by siRNA results in PCM disorganization, centriole disengagement, and centrosome amplification in the mitotic cells (**Fig. 5**), while introducing siRNA-resistant Cep57 construct rescues these phenotypes. In contrast, Cep57-FF or Cep57-KR mutants failed to rescue these phenotypes. Hence, Cep57 maintains the PCM integrity through multivalent interactions.

Collectively, this study provides crucial insights into the molecular mechanisms by which Cep57 contributes to centrosome organization through LLPS. It highlights the role of Cep57 condensates in promoting microtubule nucleation by concentrating α/β -tubulin and reveals a novel regulatory interaction where Cep63 negatively modulates Cep57's phase separation and microtubule nucleation activity. These findings enhance our understanding of the dynamic assembly of the centrosome, its regulation during cell division, and the potential implications of Cep57

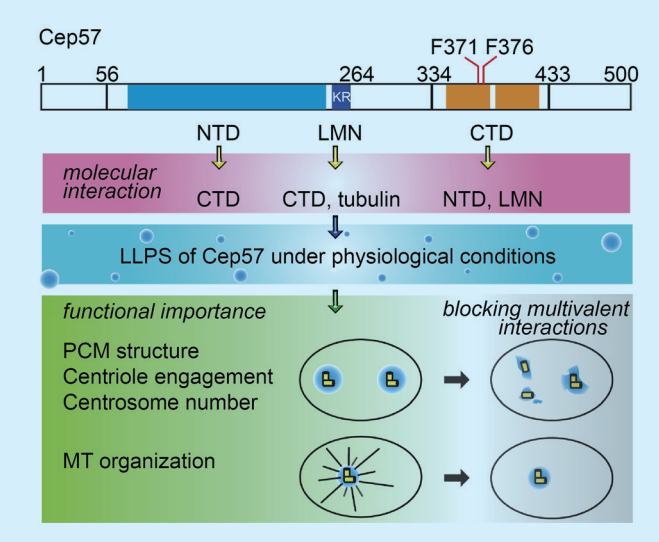


Fig. 6: A model for the assembly of human Cep57 in centrosome regulation. The domain organization of Cep57 is depicted with interactions that drive LLPS under physiological conditions. SiRNA rescue experiments reveal that the multivalent interactions of Cep57 are essential for PCM organization, and the polybasic LMN (LLPS and Microtubule Nucleation) motif facilitates microtubule aster formation. [Reproduced from Ref. 1]

mutations in centrosome-related pathologies, such as mosaic-variegated aneuploidy syndrome. (Reported by Hui-Chun Cheng, National Tsing Hua University)

This report features the work of Hui-Chun Cheng and her collaborators published in PNAS 121, e2305260121 (2024).

TPS 13A Biological Small-angle X-ray Scattering

- Biological Small/Wide Angle X-ray Scattering
- Biological Macromolecules, Structural Biology, Life Science

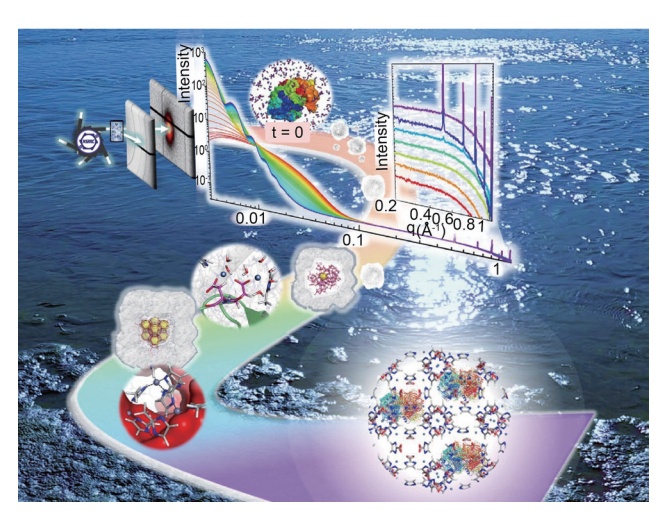
Reference

1. H. W. Yeh, P. P. Chen, T. C. Yeh, S. L. Lin, Y. T. Chen, W. P. Lin, T. Chen, J. M. Pang, K. T. Lin, L. H.-C. Wang, Y. C. Lin, O. Shih, U. S. Jeng, K. C. Hsia, H. C. Cheng, PNAS **121**, e2305260121 (2024).

Blueprints in a Drop

This research aims to revolutionize the synthesis of metal–organic frameworks (MOFs) in water by unlocking the molecular codes of biomineralization, paving the way for sustainable innovation.

etal-organic frameworks (MOFs) have emerged as superior materials for sustainable and transformative applications. Composed of metal ions and organic linkers, MOFs possess exceptional porosity and tunability, making them ideal for diverse uses such as energy conversion, catalysis, water harvesting, and biosensing. However, traditional MOF synthesis methods often rely on organic solvents, raising environmental concerns and hindering scalability and bio applications. Water-based methods for producing zirconium-based and zeolitic MOFs offer significant environmental and economic benefits while enabling the incorporation of biomolecules such as DNA and proteins. Fa-Kun Shei (National Central University) and his team focus on improving protein encapsulation efficiency within MOFs, addressing a critical challenge for expanding their practical applications.1,2



The Protein@ZIF-8 Crystallization Journey

Water's dual role in facilitating proton transfer while suppressing undesired reactions adds complexity to MOF nucleation and crystallization. To address this, Hsiao-Ching Yang's team (Fu Jen Catholic University) has developed a ground-breaking approach to elucidate water's critical role in reaction pathways. Through all-atom molecular dynamics simulations and quantum dynamics calculations, they investigated proton transfer mechanisms and structural evolution during MOF formation, uncovering essential molecular-level insights into factors influencing protein encapsulation. To validate their theoretical findings, Yang collaborated with U-Ser Jeng (NSRRC) and his team at the **TPS 13A** beamline, successfully bridging computation structures with experimental data.³

Accordingly, the interdisciplinary to transdisciplinary teamwork led by Shei, Jeng, and Yang launched a collaborative effort to explore the biomimetic nucleation and crystallization journey using ZIF-8, a zeolitic imidazolate framework, as a model system.³ Through combining advanced techniques such as in situ small-/wideangle X-ray scattering (SWAXS), multiscale simulations, and quantum calculations, the team meticulously tracked the overall process of nucleation and crystallization of ZIF-8 in aqueous solutions in real-time. This complementary approach of all-atom molecular dynamics simulations and experimental observation offered a comprehensive understanding of the molecular blueprint underlying MOF formation, decoding the ZIF-8 nucleation and crystallization process. Their research showed that the process unfolds in three distinct stages:

Stage I: Acidity Flip Proton Transfer Initial Assembly to Amorphous Nuclei. Water in the zinc-water complex is replaced by imidazole ligands, initiating an "acidity flip" that accelerates proton transfer. This shift drives the structural organization of zinc ions into amorphous cluster nuclei; imidazole ligands replace water molecules within zinc-water coordination complexes, forming the first blueprint of the crystalline structure and lead to the assembly of amorphous nuclei—the initial building blocks of the MOF structure. No ordered precursors or diffraction peaks were observed, marking the early aggregation of secondary building units (SBUs) into amorphous nuclei.

Stage II: Transition to Crystalline Nuclei and Ordered Structures. The amorphous nuclei undergo a critical transformation, evolving into ordered nuclei. This stage involves amorphous nuclei being consumed to form ordered mesoscale structures, overcoming energy barriers of approximately 21 kcal/mol in this rate-determining step. The emergence

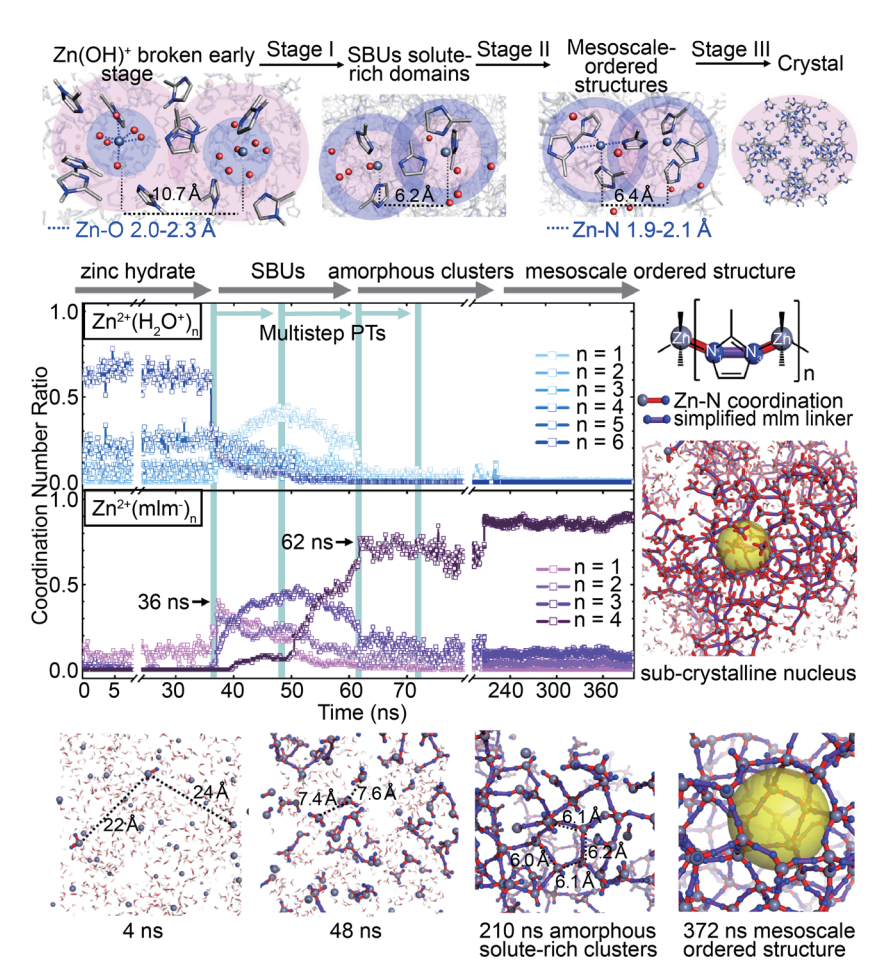


Fig. 1: MD analysis of ZIF-8 reveals a multistep Proton Transfer (PT) mechanism and structural evolution showing key Zn-O (water), Zn-N, and HmIm (N1(H), N3) interactions enabling precise protonation control with SBUs and amorphous clusters forming nucleation sites for crystalline growth in solution. [Reproduced from Ref. 3]

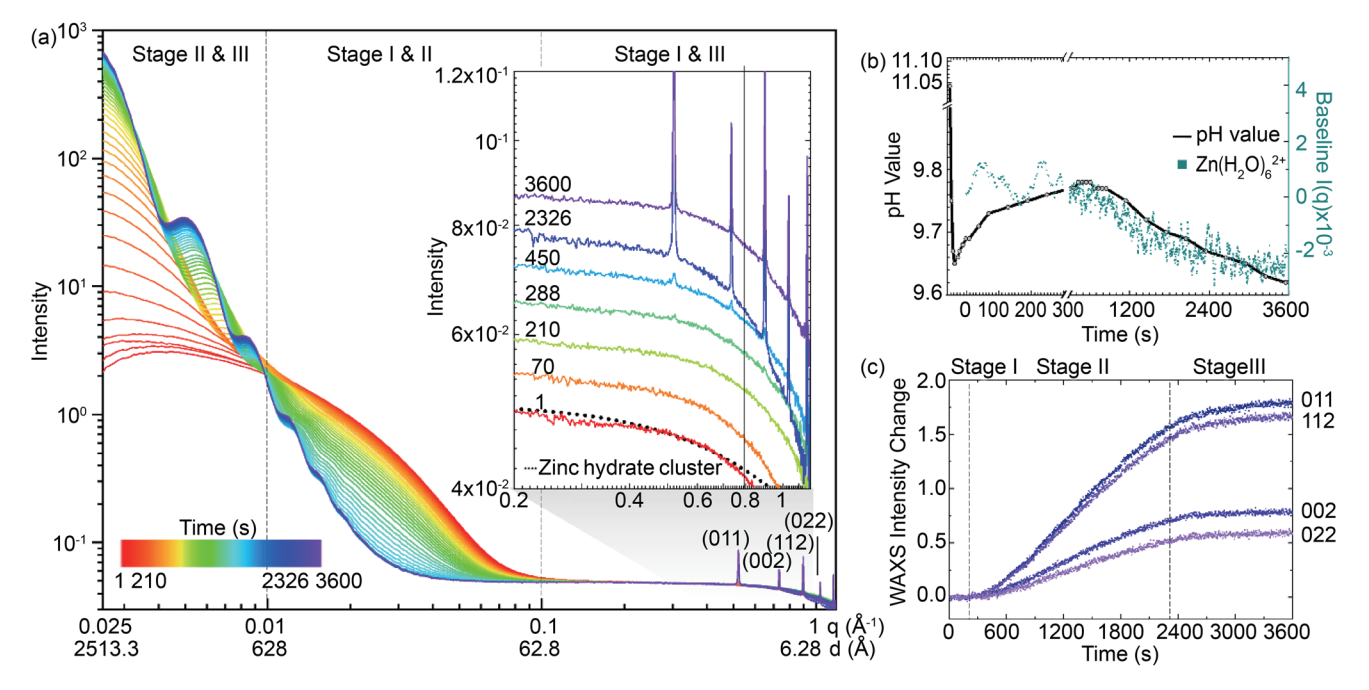


Fig. 2: In situ and operando SWAXS of ZIF-8 synthesis in aqueous solution for a HmIm/Zn²⁺ molar ratio of 1:57 at 10 °C (a) The *q*-range for scattering extends from 0.0025 to 1.2 Å⁻¹, with data acquired every second for a total duration of 3600 seconds. The inset shows an enlarged WAXS region. (b) The scattering profile baseline exhibits a clear dependence on the reaction solution's pH value. (c) The WAXS peaks corresponding to Miller indices (011), (002), (112), and (022) of ZIF-8, which all display correlated time-dependent intensity changes and can be normalized to one reference. [Reproduced from Ref. 3]

of diffraction peaks at specific q-values corresponds to the growth of crystalline nuclei, characterized by the growth of diffraction peaks at $q=0.52,\,0.74,\,0.90,\,$ and $1.04\,$ Å $^{-1},\,$ corresponding to the Miller indices (011), (002), (112), and (022), respectively.

Stage III: Formation of Stable Nanoparticles toward Crystals. Stable crystal nanoparticles emerge when molecular interactions between the crystals and the

surrounding solution reach temperature-dependent thermal equilibrium. This occurs when the structural dimensions stabilize, corresponding to the completion of the second stage. This appears to involve a temperature-dependent thermal equilibrium of the molecular interaction dynamics at the crystal–solution interface.

Biomolecular Integration in MOF EncapsulationThe results showed an inverse relationship between

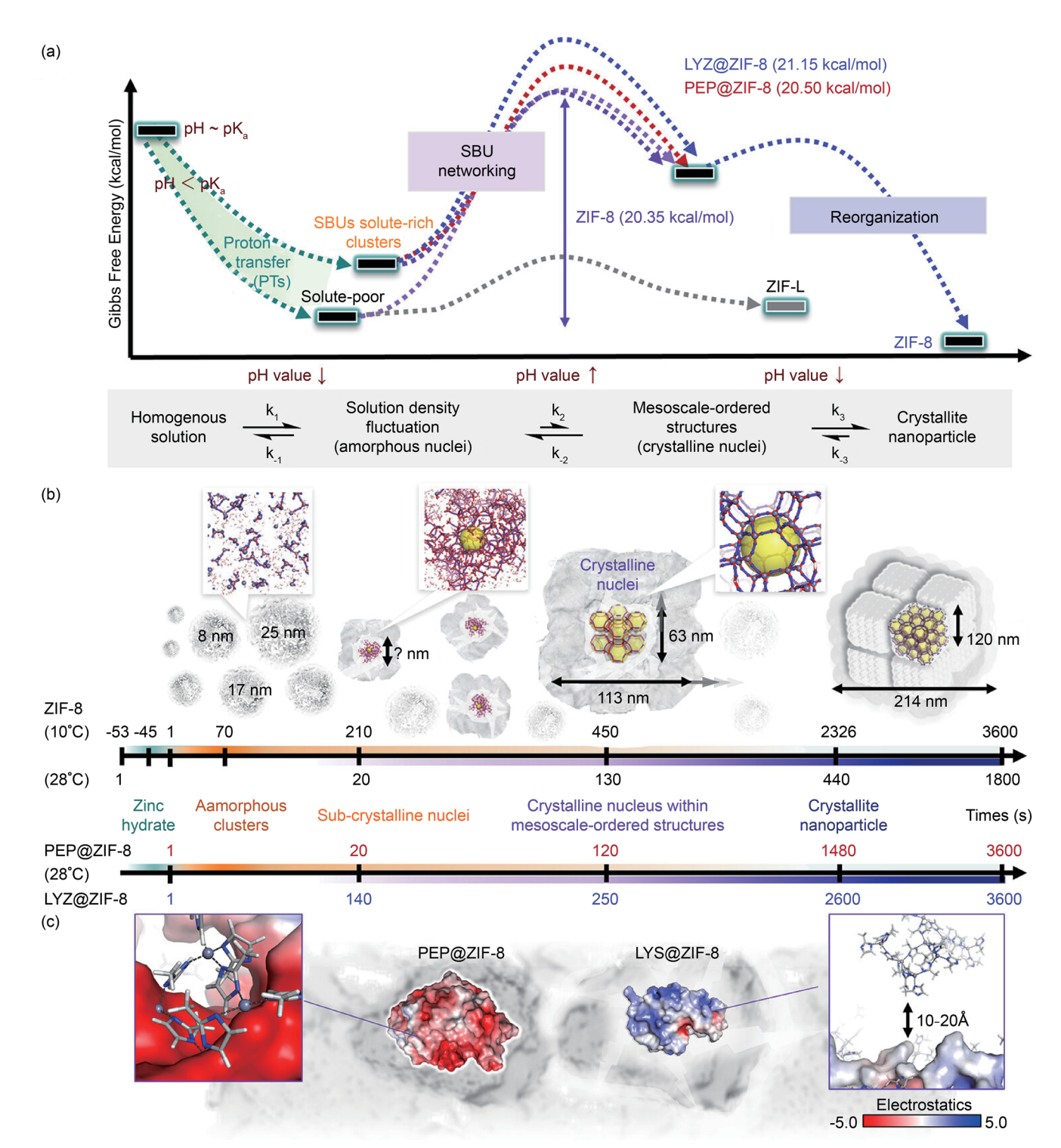


Fig. 3: In situ SWAXS reveals ZIF-8 and protein@ZIF-8 synthesis mechanisms. (a) Gibbs free energy landscapes for ZIF-8 systems. (b) Time-resolved nucleation and growth under various conditions. (c) Protein effects: PEP (negative, red) binds strongly, while LYZ (positive, blue) shows poor interaction due to electrostatic repulsion. [Reproduced from Ref. 3]

temperature and particle size. Experimental data showed that as the temperature increased from 10 to 28 °C, the microcrystal size (D 011) decreased from 139 to 80 nm, while the nanoparticle size decreased from 337 to 97 nm. This phenomenon is mainly attributed to the increased nucleation rate at higher temperatures. With the formation of more crystalline nuclei, the available reactants are distributed among more growing particles, resulting in smaller final particle sizes. Further innovation emerged from studying the effects of biomolecules on MOF formation. By incorporating proteins such as pepsin and lysozyme, researchers demonstrated that amino acid proton transfer ability and concentration directly influence the morphology and encapsulation efficiency of biomolecule-MOF composites. This study identified how proteins act as nucleation sites within amorphous MOF structures. These insights not only advance our understanding of biomineralization but also hint at designing proteins as nucleation sites for amorphous MOF growth.

In summary, this transdisciplinary research offers profound insights into the molecular mechanisms of biomimetic mineralization, where biological principles inspire synthetic material design. The findings pave the way for designing tailored MOF systems for applications. By bridging computational modeling simulations and experimental validation, this study provides a comprehensive "blueprint in a drop"—a molecular-level precision for understanding and optimizing MOF formation. By mastering these

microscopic processes, the team unlocks more sustainable and innovative applications in fields ranging from energy storage to pharmaceuticals. The journey from a single aqueous drop to a complex crystalline network underscores the profound potential of small beginnings in shaping the advanced materials of the future. (Reported by Hsiao-Ching Yang, Fu Jen Catholic University)

This report features the work of Hsiao-Ching Yang and her collaborators published in ACS Nano 18, 25170 (2024).

TPS 13A Biological Small-angle X-ray Scattering

- In situ SWAXS
- Physical Chemistry, Chemical Physics, Computation Chemistry, Materials Science, Aqueous Chemistry

References

- S.-Y. Chen, W.-S. Lo, Y.-D. Huang, X. Si, F.-S. Liao, S.-W. Lin, B. P. Williams, T.-Q. Sun, H.-W. Lin, Y. An, T. Sun, Y. Ma, H.-C. Yang, L.-Y. Chou, F.-K. Shieh, C.-K. Tsung, Nano Lett. 20, 6630 (2020).
- P. K. Lam, T. H. Vo, J.-H. Chen, S.-W. Lin, C.-L. Kuo, J.-J. Liao, K.-Y. Chen, S.-R. Huang, D. Li, Y.-H. Chang, H.-Y. Chen, H.-T. Hsieh, Y.-A. Hsu, H.-K. Tsao, H.-C. Yang, F.-K. Shieh, J. Mater. Chem. A 11, 24678 (2023).
- 3. S.-W. Lin, P. K. Lam, C.-T. Wu, K.-H. Su, C.-F. Sung, S.-R. Huang, J.-W. Chang, O. Shih, Y.-Q. Yeh, T. H. Vo, H.-K. Tsao, H.-T. Hsieh, U-S. Jeng, F.-K. Shieh, H.-C. Yang, ACS nano 18, 25170 (2024).

Unlocking Hydrogen Power with Single-Atom Pt Catalysts

3D hierarchically organized metal single atoms have attracted considerable attention for their high efficiency in various catalytic reactions.

Single-atom catalysts have garnered significant attention because of their exceptional activity and efficiency across a broad spectrum of catalytic reactions. However, developing stable single-atom catalysts and cocatalysts that maintain high performance presents significant challenges, particularly in achieving uniform dispersion, stabilization, and a sufficiently high density of single-atom sites. Currently, the majority of reported single-atom catalysts have predominantly been achieved using two-dimensional substrates lacking steric infrastructures. The dispersion of these single-atom catalysts relies heavily on their adsorption or coordination with substrates, such as carbon blacks or graphene surfaces. These weak interactions struggle to counteract the aggregation of single-atom catalysts into nanoparticles during catalytic reactions, leading to suboptimal performance.

Recent studies have suggested the potential use of metal–organic frameworks (MOFs) to create three-dimensional (3D) hierarchical structures, thus allowing the deployment of catalysts/cocatalysts inside MOF cages through diffusion or onsite reduction. This approach aims to mitigate the aggregation effect of single atoms, thereby sustaining their performance. However, achieving a uniform deposition of single catalysts/cocatalysts throughout the deep inner MOF cages presents a significant challenge.

U-Ser Jeng and his team at the NSRRC recently developed a method that involves embedding single platinum (Pt) atoms within silicate nanochannels for a paired single-atom cocatalyst and catalyst to achieve efficient and stable photocatalytic centers of a high number density in 3D substrates. Using phosphotungstic acids (PTAs) as templates, they achieved a high loading of single Pt atoms (3.0 wt%). Advanced techniques, including X-ray absorption spectroscopy (TPS 44A)² and electron microscopy, revealed that Pt atoms are stabilized via four-oxygen coordination within PTA, effectively reducing the energy-driving aggregation (Fig. 1). This system's design relies on controlling the ratio of Pt atoms to PTA. A critical ratio of 3.7 ensures nearly pure single-atom dispersion. At higher ratios, Pt clustering becomes evident. The research team used a three-stage solution synthesis process of template formation, Pt adsorption, and reduction at the air-liquid interface to create this unique structure. In situ grazing-incidence small-angle scattering (GISAXS) measurements (TLS 23A1 and TPS 13A)3,4 and thermogravimetric analyses demonstrated that increasing PTA content enhanced single-atom dispersion, while excessive PTA led to structural deterioration. The resulting Pt-PTA pairs within silicate nanochannels exhibit the outstanding hydrogen evolution reaction (HER) efficiency, achieving a hydrogen production rate of 300 mmol/h/g Pt, which is double that of previous systems. The PTA's empty tungsten d shell facilitates photoexcited electron transfer to Pt, enabling efficient hydrogen reduction. The nanochannels also prevent Pt clustering and sustain long-term performance. This breakthrough establishes a record-high Pt efficiency for HER among polyoxometalate (POM)-based systems. The 3D-ordered structure stabilizes single Pt atoms and creates a synergistic network for enhanced charge transfer. This innovative strategy highlights the potential for developing robust, high-performance single-atom catalysts for energy applications.

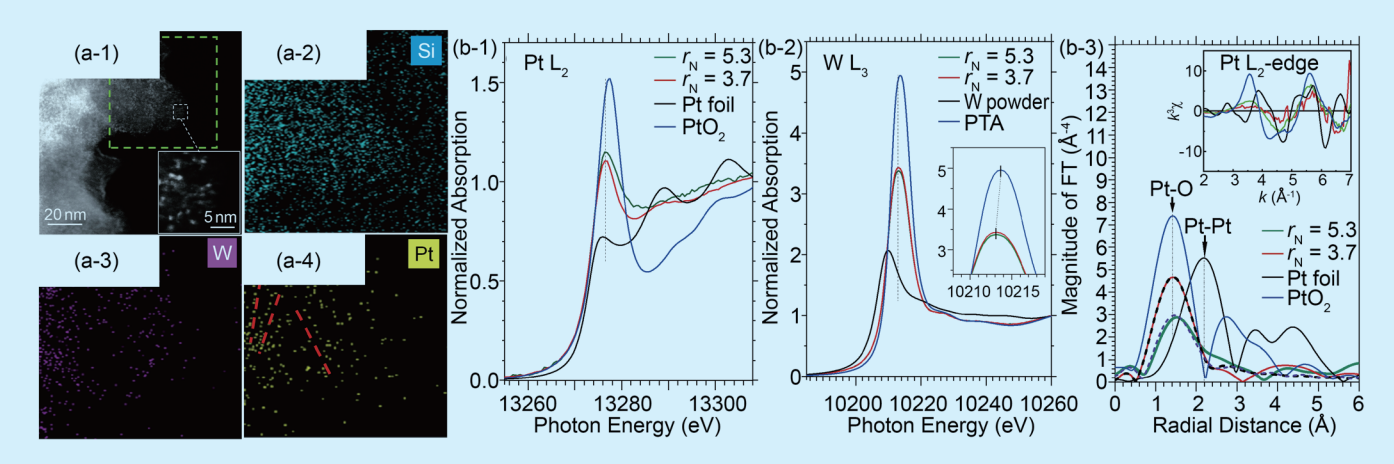


Fig. 1: (a-1) High-angle annular dark field-scanning transmission electron microscopy (HAADF–STEM) image of a typical zone on Pt–PTA within the silicate nanochannels of a low Pt atom/PTA number ratio, r_N , of 5.3; the inset (white square) zooms in on the local details, with the dispersed bright spots contributed by the scattering from heavier elements of Pt and W in the sample. Corresponding energy-dispersive X-ray spectroscopy (EDS) maps of (a-2) Si, (a-3) W, and (a-4) Pt, taken from the sample zone marked by the green dotted frame in (a-1). (b-1–3) X-ray absorption spectra measured at the (b-1) Pt L₂-edge and (b-2) W L₃-edge for the two samples of Pt–PTA within silicate nanochannels, with r_N = 5.3 and 3.7. Also shown are the spectra of Pt foil (measured in transmission mode), PtO₂, and tungsten and PTA powders for comparison. (b-3) Fourier transform of the samples and the references (with no phase corrections). The inset shows the corresponding (same colors) Pt L₂-edge k³-weight extended X-ray absorption fine structure (EXAFS) spectra. The data with r_N = 3.7 (or 5.3) are respectively fitted with the dotted (or dashed) curve by using a mean first-shell coordination number Nc = 3.88 (or 2.6) and a Pt–O bond length R = 1.93 Å (or 1.96 Å). [Reproduced from Ref. 5]

From the HER and X-ray absorption spectroscopy (XAS) results, Pt single atoms in Pt_1 –PTA pair coordination within the arrayed silicate nanochannels outperform Pt nanoparticles with PTA in the same environment by fourfold efficiency (**Fig. 2(a)**, see next page). Such one-to-one Pt_1 –PTA pair coordination has many advantages in the photoelectric conversion of HER *via* metal-to-metal charge-transfer excitation. In this process, the WO₃-based PTA (having an empty d shell with tungsten W⁶⁺ in $5d^0$ configuration) provides photoexcited electrons, with the states of W⁵⁺ in $5d^1$ configuration to the coordinated Pt_1 for hydrogen reduction. The PTA-4H site provides Pt_1 a stable absorption and four coordinated oxygen atoms for an oxidation state of ca. +2 (as revealed from the XAS and discrete Fourier transform calculation results). The median oxidation state of Pt_1 presumably is favorable for serving as a co-catalyst to accept photoelectrons from PTA and subsequently transfer the electrons to nearby protons for HER. The hydrogen adsorption energy Pt_1 of Pt_2 and subsequently transfer the electrons to nearby protons for HER. The hydrogen adsorption energy Pt_2 faster, easier hydrogen desorption after reduction. These advantages render the Pt_1 of the Pt_1 -PTA pair an efficient co-catalyst in the photocatalytic HER mechanism. On top of the high HER efficiency within the Pt_1 -PTA pair, the 3D network of a high number density of Pt_1 -PTA pairs organized *via* the arrayed silicate nanochannels can further synergistically convert near neighbors' photoelectrons available within the network and those contributed by the PTA in the HER solution. Moreover, the nanochannel pore

structure (ca. 2 nm channel pore size) with densely intercalated PTA (ca. 1 nm size) suppresses the clustering of the channel Pt_1 during catalytic reactions for sustainable performance. With all these advantages, this new hierarchical structure achieves a record high Pt efficiency in HER among the POM-based photocatalytic systems. It may be considered an efficient electrode material in photoelectrochemical cells.

In summary, the team successfully developed a three-stage synthesis process at the air-liquid interface, enabling precise control over the deposition and dispersion of platinum atoms (Pt₁) within hexagonally packed

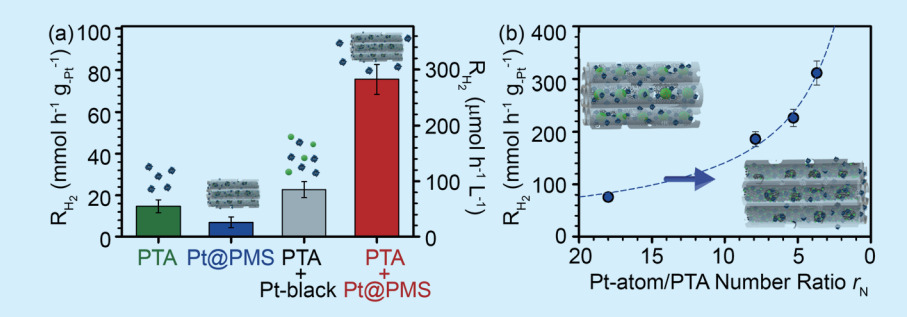


Fig. 2: (a) H₂ production rate measured for a 100 mL solution containing 5 mg of the nanocomposite of Pt–PTA within silicate nanochannels (r_N =18), 1.2 mM PTA, 0.2 M H₂SO₄, and isopropanol (20% vol.). Also shown are the H₂ production rates measured in similar solutions for the nanocomposite, solely PTA, and Pt black (of an equal Pt weight) suspension, in similar PTA solutions, as illustrated by the illustrations. (b) Increase in the H₂ production rate with the reduction of r_N of the nanocomposite with increasingly more Pt₁–PTA pairs; inset illustrations show the corresponding transition of Pt dispersion from nanoparticles (left) to Pt₁ on PTA (right) within the arrayed silicate nanochannels. [Reproduced from Ref. 5]

silicate nanochannels. This approach achieved an efficient Pt₁–PTA configuration, demonstrating record-high performance in HER. The outstanding performance of this structure is attributed to the stable 4H-site coordination, enhanced electron transfer efficiency, high-density Pt₁–PTA pairs, and exceptional anti-clustering properties. Moreover, the integration of synchrotron radiation techniques, such as GISAXS and XAS, played a pivotal role in providing high-sensitivity *in situ* analysis, allowing a detailed understanding of the formation mechanism, structural characteristics, and reaction dynamics of Pt₁–PTA pairs within the nanochannels. These advanced characterization methods offered critical data for the experimental process and provided valuable insights for designing and optimizing 3D single-atom catalysts. This study highlights the potential of combining synchrotron radiation capabilities with advanced synthesis techniques to develop highly stable and efficient single-atom catalysts. It paves the way for innovative applications in photochemical and renewable energy conversion systems. (Reported by Je-Wei Chang)

This report features the work of U-Ser Jeng and his collaborators published in ACS Nano 18, 1611 (2024).

TPS 13A Biological Small-angle X-ray Scattering TPS 44A Quick-scanning X-ray Absorption Spectroscopy TLS 23A1 Small/Wide Angle X-ray Scattering

- GISAXS, NEXAFS, WAXS
- Materials Science, Chemistry, Surface, Interface and Thin-film Chemistry, Condensed-matter Physics

References

- 1. X. F. Yang, A. Wang, B. Qiao, J. Li, J. Liu, T. Zhang, Acc. Chem. Res. 46, 1740 (2013).
- 2. C.-W. Pao, J. L. Chen, J. F. Lee, M. C. Che, C. Y. Huang, C. C. Chiu, C. Y. Chang, L. C. Chiang, Y. S. Huang, J. Synchrotron Radiat. 28, 930 (2021).
- 3. U.-S. Jeng, C. H. Su, C.-J. Su, K.-F. Liao, W.-T. Chuang, Y.-H. Lai, J.-W. Chang, Y.-J. Chen, Y.-S. Huang, M.-T. Lee, K.-L. Yu, J.-M. Lin, D.-G. Liu, C.-F. Chang, C.-Y. Liu, C.-H. Chang, K. S. Liang, J. Appl. Crystallogr. 43, 110 (2010).
- 4. O. Shih, K. F. Liao, Y. Q. Yeh, C. J. Su, C. A. Wang, J. W. Chang, W. R. Wu, C. C. Liang, C. Y. Lin, T. H. Lee, C. H. Chang, L. C. Chiang, C. F. Chang, D. G. Liu, M. H. Lee, C. Y. Liu, T. W. Hsu, B. Mansel, M. C. Ho, C. Y. Shu, F. Lee, E. Yen, T. C. Lin, U. Jeng, J. Appl. Crystallogr. 55, 340 (2022).
- 5. J. W. Chang, K. H. Su, C. W. Pao, J. J. Tsai, C. J. Su, J. L. Chen, L. M. Lyu, C. H. Kuo, A. C. Su, H. C. Yang, Y. H. Lai, U. S. Jeng, ACS Nano 18, 1611 (2024).